# Open-Loop Dynamics of the Asymmetric Vortex Wake behind a von Kármán Ogive at High Incidence

**Casey Fagley[1], John Farnsworth[1], Chris Porter[1], Jürgen Seidel[1], Thomas McLaughlin[1], Jinik Lee[2] and Eunseok Lee[2]**
[1]Department of Aeronautics, U.S. Air Force Academy, Colorado Springs, CO 80840, USA
[2]Agency for Defense Development, Daejeon, Republic of Korea

Received date 27th November 2012; Accepted date 28th February 2013

**Abstract**
The asymmetric vortex regime of a von Kármán ogive with fineness ratio of 3.5 is experimentally studied at a Reynolds number of 156,000. Both port and starboard plasma actuators are used to introduce fluidic disturbances at the tip of the ogive which are amplified through the flow's convective instability and produce a deterministic port or starboard asymmetric vortex state (i.e. side force). Accurate control or manipulation of this asymmetric vortex state holds the potential for increased maneuverability and stability characteristics of slender flight vehicles at high angle of attack. Open-loop experimental tests are used to understand and quantify the vortex dynamics due to actuation inputs. Linear time invariant models provide a suitable model structure to replicate the vortex dynamics and allow for simulation and closed-loop control design. Standard PID control is designed and implemented. A closed-loop simulation shows arbitrary side force tracking with adequate disturbance rejection.

## NOMENCLATURE

| | |
|---|---|
| $C_P$ | Pressure coefficient |
| $D$ | Diameter |
| $f_r$ | Fineness ratio, $L_{cone}/D$ |
| $L_{aft}$ | Aft body length |
| $L_{cone}$ | Nose cone length |
| $M$ | Mach number |
| $Re$ | Reynolds number, $U_\infty D/\nu$ |
| $\tau$ | Dimensionless time, $L_{cone}t\ /U_\infty$ |
| $U_\infty$ | Wind tunnel free-stream velocity |
| $\alpha$ | Angle of attack |
| $\Delta C_P$ | Differential pressure coefficient, port - starboard |
| $\theta$ | Azimuthal position |

## 1. INTRODUCTION

The flow field around a slender, axisymmetric forebody varies dramatically with the angle of attack. Typically, four flow regimes are observed: attached flow ($0° \le \alpha < 15°$), symmetric vortex flow ($15° \le \alpha < 40°$), asymmetric vortex flow ($40° \le \alpha < 60°$), and unsteady wake-like flow ($\alpha \ge 60°$) [9, 11, 16]. Illustrations of these flow regimes are shown Fig. 1. The transition between the symmetric and asymmetric vortex flow is due to an instability of the natural flow field. Minor geometric imperfections and flow perturbations are amplified by this convective instability and divert the flow field away from the symmetric vortex state into an asymmetric vortex state in which either port or starboard vortex will separate from the forebody surface and cause a large asymmetric pressure distribution on the ogive surface.

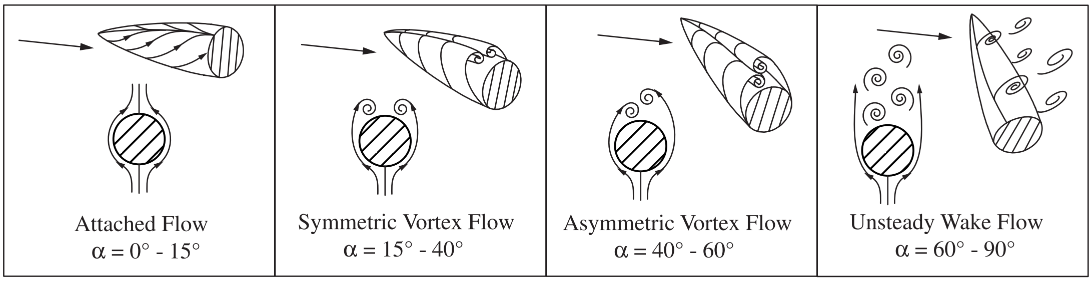


Figure 1: Flow state on a tangent-ogive forebody as a function of angle of attack.

Once this occurs, the asymmetric vortex state produces a significant side force on the body, typically on the order of 40% to 70% of the normal force depending on angle of attack. This side force or phantom yaw is a detrimental problem for the stability and maneuverability characteristics of slender flight vehicles at high incidence [4, 10, 18]. Numerous experimental and numerical investigations for a range of geometric shapes and Reynolds numbers have been performed to understand this phenomenon.

The natural tendency of the flow field to favor an asymmetric vortex state emphasizes the importance of forebody vortex management. A variety of different flow control methods have been devised for different forebody configurations. Typically, passive control techniques, in which no energy is added to the flow, make use of nose strakes, dimples, nose blunting, and other geometric modifications to reduce the flow's instability and enforce a symmetric vortex state [21, 4, 7]. For example, Cui et al. sought to enforce a symmetric vortex configuration (i.e regulation of side force) at higher angles of attack by adding dimples to the forebody [6]. The energized, turbulent boundary layer induced symmetric separation locations along the ogive surface and suppressed asymmetric vortex formulation up to an angle of 55°, at which point the instability overcame the passive control and the flow resumed the asymmetric behavior. This passive control study supports that vortex management is achieved via manipulation of the separation location. On the other hand, Degani performed numerical simulations studying the effect of a geometric disturbance on asymmetric vortex states [8]. The simulations for a smooth geometry predicted a symmetric state while the addition of a very small geometric disturbance (e.g. a bump on the order of the boundary layer thickness) toward the apex or nose of the forebody favored an asymmetric vortex formation. This passive control technique supports that vortex management is receptive to surface disturbance, but does not indicate the mechanism responsible for vortex manipulation (i.e. either vorticity or momentum addition). These mechanisms need to be considered for the successful control of vortex dynamics.

Open-loop active flow control methods, in which energy is added to the flow, make use of a fluidic actuator (plasma, blowing and suction ports, synthetic jets, etc.) near the nose of the forebody. This has been shown to be the best location for actuation to utilize the convective instability and yield the largest disturbance growth in the flow [3]. Open-loop studies varying the disturbance strength (i.e. actuation parameters such as frequency, amplitude and actuator orientation) are used to quantify the vortex dynamics. For example Bernhardt et al. showed a proportional relationship at $\alpha = 45°$ between the amount of vortex asymmetry and the actuation amplitude, Fig. 2a. The authors also showed that at larger angles of attack the effect of the instability increases and results in a bistable system, as shown in Fig. 2b. While these results were shown for small Reynolds numbers, Re = 6,300, the authors also showed that at larger Reynolds numbers the bistable nature of the vortex dynamics was not present; instead, their results indicate that the side force is proportional to the control input [1].

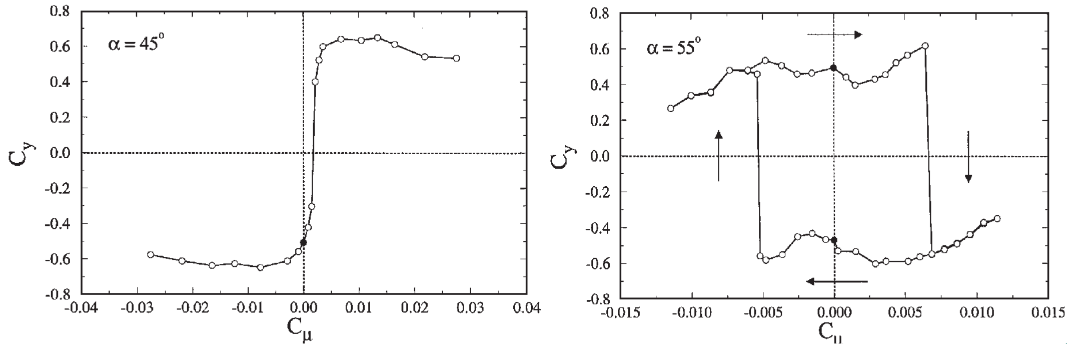


(a) Proportional system (b) Bi-stable system

Figure 2: Open-loop forcing with varying actuation amplitude shows limited proportional (a) and bistable (b) systems at $\alpha$ = 45° and 55° [2].

To improve vortex management performance with respect to open-loop methods, closed-loop active control techniques, in which sensor signals are used to estimate the flow state and then prescribe the actuation input to reach a desired state, hold the promise to increase stability and maneuverability characteristics for high angles of attack at varying flow conditions. Active closed-loop flow control presents the opportunity to not only regulate side force with better performance than current open-loop techniques, but also allow for the possibility to attain attitude control of a slender body via active vortex manipulation. However, to date very little research has been performed exploiting the full potential of feedback flow control on forebodies. Bernhardt and Williams focused on regulating the side force at a range of angles of attack through the use of active closed-loop control. According to their report, the highly unstable oscillatory response of the flow at higher angles of attack exceeded the actuator and hardware dynamical ranges. The researchers had limited success enforcing symmetric vortex states for $\alpha > 48°$ [3].

Bernhardt and Williams' experiment encountered a very limited frequency response because of the time delay in the experiment. A large portion of their time delay was attributed to the mechanical implementation of the bleed actuators, but a significant portion is also accounted for by the transition and development of the flow field [3]. Finally, Patel et al. were able to close the loop on the forebody and control side force using mechanically deployable flow effectors (DFEs). However, prior to accomplishing the closed-loop control they found in open-loop tests that statically deployed DFEs produced the largest side forces and that the control effectiveness diminished by increasing the oscillation frequency of the DFEs. From this they concluded that the time scales associated with the development and propagation of the vortices is critical in obtaining the desired level of side force [22]. Clearly, the dynamics and time scales of the vortex system need to be well understood to successfully accomplish closed-loop control on a slender forebody.

The necessary energy to achieve effective feedback flow control is small in comparison to the potential gain because of the exploitation of the flowfield's convective instability. Through precise disturbance introduction at the nose of the forebody and dynamic measurements on the surface of the ogive, control algorithms can be formulated such that arbitrary side force trajectories can be adequately followed. For fluidic actuation, two single dielectric barrier discharge (SDBD) plasma actuators are employed to swap the vortex states on the forebody. Plasma actuators offer several advantages as a flow control effector; the primary advantage is the very high frequency response [12, 14]. SDBD plasma actuators also have no moving parts and rely solely on the transmission of electrical energy. This electrohydrodynamic mechanism operates at the time scale of electron collisions (on the order of nano seconds) which is orders of magnitude faster than any dynamics in the flow field. Thus, plasma actuation provides a means to achieve higher closed-loop performance in comparison to the other closed-loop actuation methods applied to the asymmetric vortex problem.

Before closed-loop control of the vortex asymmetry can be achieved, a complete understanding of the unforced and open-loop dynamics is needed to intelligently lead the control design. In this paper, the necessary steps are described. First, a database consisting of unforced and open-loop forced measurements is gathered. Then, the effectiveness to capture the relevant fluid dynamics of various modeling techniques such as output error, prediction error and subspace identification methods are compared on the experimental database. Finally, model performance is shown and, in conjunction, the system dynamics of the asymmetric vortex problem is well modeled by a linear transfer function. The developed low dimensional models provide for control design which is then simulated as an output disturbance problem.

## 2. SETUP

### 2.1 Geometry

The geometry considered in this investigation is a generic von Kármán ogive which is a part of the Haack series nose cones with fineness ratio $f_r = 3.5$ and a diameter of $D = 0.1$ m. The nose cone shape is computed from Eqs. (1) and (2), where the origin of the coordinate system is at the nose of the model.

$$\theta_o = \arccos\left(1 - \frac{2x}{L_{cone}}\right) \tag{1}$$

$$r = \frac{D\sqrt{\theta_o - \frac{\sin(2\theta_o)}{2}}}{2\sqrt{\pi}} \tag{2}$$

A cylindrical aft body with length $L_{aft} = 0.05$ m is added to the end of the ogive forebody. Figure 3a shows the geometry and defines coordinate system for this study. The model was fabricated in multiple sections using a 3D stereolithography (SLA) printer.

### 2.2 Experimental Setup

The experimental tests on the ogive model were conducted in the North Low Speed Wind Tunnel in the Aeronautics Laboratory at the U.S. Air Force Academy. The wind tunnel has a speed range from 3 m/s to 30 m/s, a test section of 0.91 m x 0.91 m x 2.29 m, a power rating of 19.5 kW, a turbulence intensity of 0.15%, and was manufactured by Engineering Laboratory Design Inc. For the tests discussed, the tunnel velocity is $U_\infty = 30$ m/s, which leads to a Reynolds number based on maximum ogive diameter of $Re = 156{,}000$. Additionally, the model was placed at a constant angle of attack of $\alpha = 50°$.

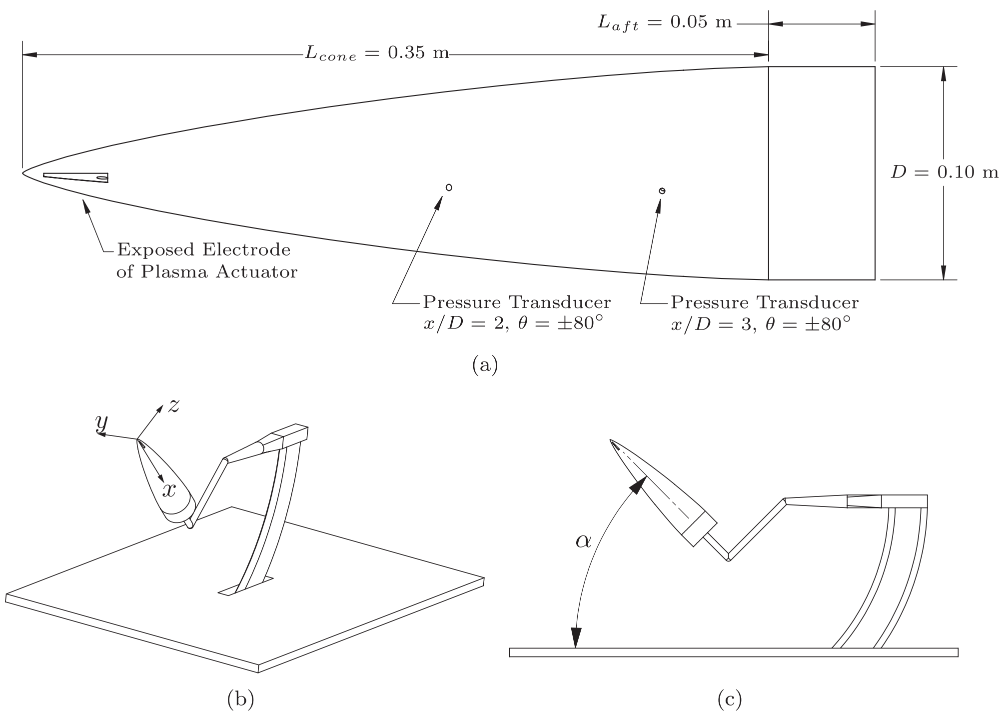


Figure 3: Schematic drawings of von Kármán ogive model.

Multiple measurements were made simultaneously during the experiments including six degree of freedom force-moment measurements and surface pressure measurements. A 10-lb Mini-6 moment balance from NK Biotechnical Corporation was utilized to measure the aerodynamic forces and moments on the model. The balance signals were amplified by a gain of 1000 and low-pass filtered at 1 kHz through a Dynamics 7914AR/NR model signal conditioner before being measured by a National Instruments PCI 6071E multfunction data acquisition board. The resultant normal (i.e. pitch direction) and side (i.e. yaw direction) forces, as well as the average pitch and yaw moments are reduced at the balance moment reference center, $x/D = 2.66$.

Four Endevco 8507C piezoresistive pressure transducers were mounted in the model flush to the surface at $x/D = 2$ and 3 at $\theta = \pm 80°$ from the forward meridian line on the tangent ogive model as detailed in Fig. 3. Each of the pressure transducers had a range of ±2 psi (±13.8 kPa), a sensitivity of approximately 160 mV/psi (23.2 mV/kPa), and resonant frequency of 60 kHz. The transducers have an approximate uncertainty of 1.5% of the full scale output, or ±0.03 psi (±0.2 kPa). The pressure transducer signals were amplified by a gain of 500 and low-pass filtered at 1 kHz through a Dynamics 7914AR/NR model signal conditioner before being measured by a National Instruments cRIO-9074 integrated realtime controller and FPGA device. The sectional differential pressure coefficient, $\Delta C_P$, presented below is the difference between the pressure coefficients, $C_P$, measured on the starboard and port sides of the model. They are defined by Eqs. (3) and (4)

$$C_{P_i} = \frac{P_i - P_\infty}{\frac{1}{2}\rho U_\infty^2} \tag{3}$$

$$\Delta C_P = C_{P_{Port}} - C_{P_{Starboard}} = \frac{P_{Port} - P_{Starboard}}{\frac{1}{2}\rho U_\infty^2}. \tag{4}$$

The sensor placement was determined through an optimal genetic algorithm as documented by Fagley et al. [13]. The optimal placement of sensors located them near the maximum spatial variation of the separation location, such that the pressure difference from left to right asymmetric vortex states was maximized. This arrangement of sensors minimized the linear estimation between the four pressure transducer measurements and side force measurements in forced and unforced CFD simulations. The estimated force is computed by the linear model,

$$\hat{C}_y(t) = CP_i(\mathbf{x_s}, t), \tag{5}$$

where $P_i$ ($\mathbf{x_s}$, $t$) is the vector of pressure measurements at surface locations $\mathbf{x}_s$, $C$ is the vector of coefficients which map pressure measurements into the estimated side force, $\hat{C}_y$.

## 2.3 Plasma Actuation

Single dielectric barrier discharge (SDBD) plasma actuators, a recent development in flow control technology, provide sufficiently large frequency response as well as adequate disturbance amplitude to control the asymmetric vortex behavior. Briefly, a SDBD plasma actuator consists of two electrodes separated by a dielectric material [5]. One of the electrodes is typically exposed to the surrounding gas. Alternating current at frequencies ranging from 200 Hz to 25 kHz and voltages of 5kVpp or larger ionizes the air and forms a plasma. The plasma collects on the dielectric material at the location of the highest electric field potential inducing a small mass flow for half of a duty cycle of the AC current in the direction of the plasma [5, 19, 20, 23]. Plasma actuators have been used for numerous flow control applications such as laminar to turbulent transition [15], leading edge separation control [17], low Reynolds number airfoil flows [24], shear layer instabilities [24], flow past a backward facing step [25], and many more.

The challenge for implementation of a SDBD actuator for the von Kármán ogive is in creating a surface mounted actuator without producing a significant geometric disturbance on the model surface, as it has been shown in the literature that the vortex state is extremely sensitive to any geometric imperfections [4]. The SDBD plasma actuators used in this paper are oriented parallel to body axis of rotation between $x/D = 0.1$ and 0.4 at $\theta = \pm 90$ as shown in Figure 4.

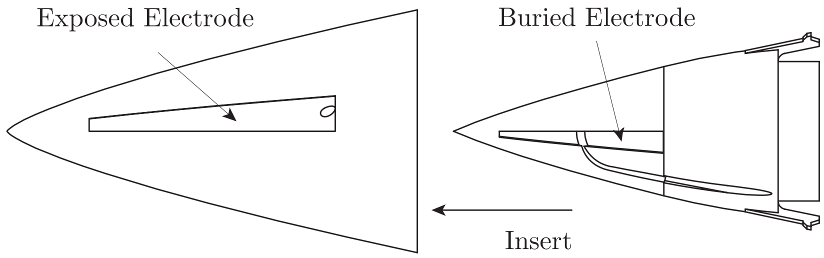


Figure 4: Schematics of the SDBD Plasma Actuator nose tip. The exposed electrode is contained on the outer shell and the buried electrode is contained on the inner insert. Both pieces are snapped together to create a very nice SDBD actuator.

This actuator design provided a stable and repeatable plasma on the surface of the ogive with minimal alterations to the von Kármán ogive shape. The actuator tip assembly was then installed on the von Kármán ogive model in an orientation such that the plasma actuators create a jet and therefore a body force on the fluid in the direction of the mean flow.

## 3. RESULTS

### 3.1. Approach

To model the system dynamics of the asymmetric vortex state behind the von Kármán ogive at high angles of attack, open-loop experimental tests were conducted to understand system characteristics in terms of stability/bi-stability, controllability, observability, and linear/non-linear behavior. The flow behind an axisymmetric slender body has previously been shown to be completely bistable at a sufficiently large angle of attack and small Reynolds numbers. Because few tests have been conducted at a Reynolds number in the range of the current experiment ($\mathrm{Re} =$ 156,000), determining if a bi-stable or proportional flow regime exists is critical in designing a suitable model structure and control system design.

As presented in [14], at the current operating conditions, the system is shown to be proportional at an incidence of 50°. Figure 5 shows a schematic of the responsiveness of the asymmetric state (measured as the resulting side force) to plasma actuation. The positive x-axis represents the port forcing strength and the negative x-axis represents the starboard forcing strength; the zero location is the unforced state. The unforced state of the asymmetric vortex configuration varies based on geometry disturbances, flow conditions, misalignments, flow imperfections etc. Around this initial state is a dead

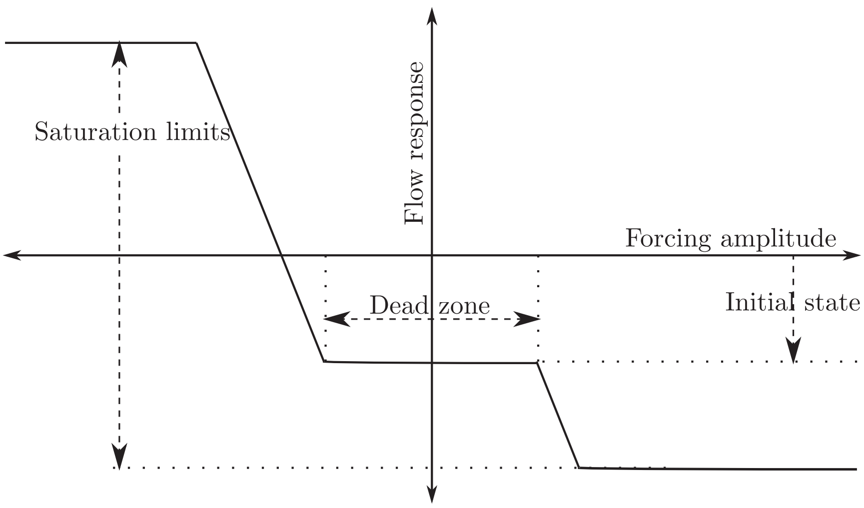


Figure 5: Representation of the forcing characteristics of the asymmetric vortex state due to plasma actua- tion.

zone in the actuator dynamics; that is, the actuation voltage must exceed a certain limit before plasma formation takes place. Above and below this region a linear response in asymmetric vortex state was found. At large enough forcing magnitudes the vortex system does saturate in the fully left or right asymmetric vortex state.

The forcing and fluidic response representation as depicted in Figure 5 is experimentally measured by side force and sectional pressure measurements. The results are shown in Figure 6. The side force, $C_y$ and sectional pressure coefficient, $\Delta C_P$, at x/D = 3 vary analogously with varying port/starboard plasma voltage which supports that time resolved pressure measurements do accurately correlate with integrated force measurements. As Figure 6 also shows, the system responds nearly proportionally, although non-linear effects are apparent. For instance, the dead zone in the actuation voltage range from $-5kV \leq V \leq 5kV$ does exist; this is, primarily due to the fact that plasma has not formed at these smaller voltage potentials. Also, a hysteresis is definitely observed, that is the path along a positive voltage gradient, $\frac{dV}{dt} > 0$, is different from the path along a negative voltage gradient, $\frac{dV}{dt} < 0$, in both time accurate (red/blue lines) and integrated measurements (black lines). Finally, a larger gradient, $\frac{d\Delta C_P}{dV}$ is seen near the symmetric vortex location ($C_y = \Delta C_P = 0$), supporting the fact that a small amount of bistability does exist at this flow condition.

The system response in Figure 6 is well modeled by a linear system with slight non-linearities present. Also, it is easy to see that the side force is suitably estimated by a linear combination of sectional pressure measurements. The flow state estimation technique laid out in [13], is experimentally verified by the following technique. The estimated side force, $\hat{C}_y$, as described by Eqn. 5, needs to be validated and compared to the actual force on the model. To compare these two signals, the force balance sensor dynamics need to be measured and modelled. For this an impulse response to the wind tunnel model and resulting forces are measured to model the frequency response. Figure 7a shows the frequency response of the side force measurement due to an impulse. A multi-modal resonance is seen due to the complex orientation of strain gauge/flexure arrangement of the 6 degree of freedom force balance; additionally, each balance channel shows a cross coupled behavior which is also a factor for the multi-modal resonance.

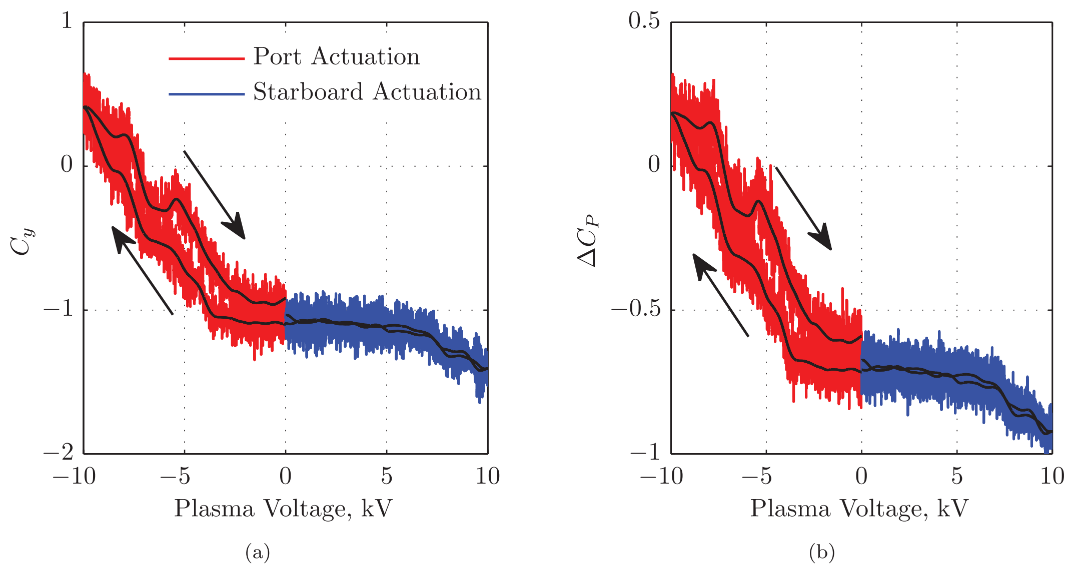


Figure 6: (a) Side force coefficient and (b) differential pressure coefficient at x/D = 3 versus the plasma actuator voltage during the ramp modulation.

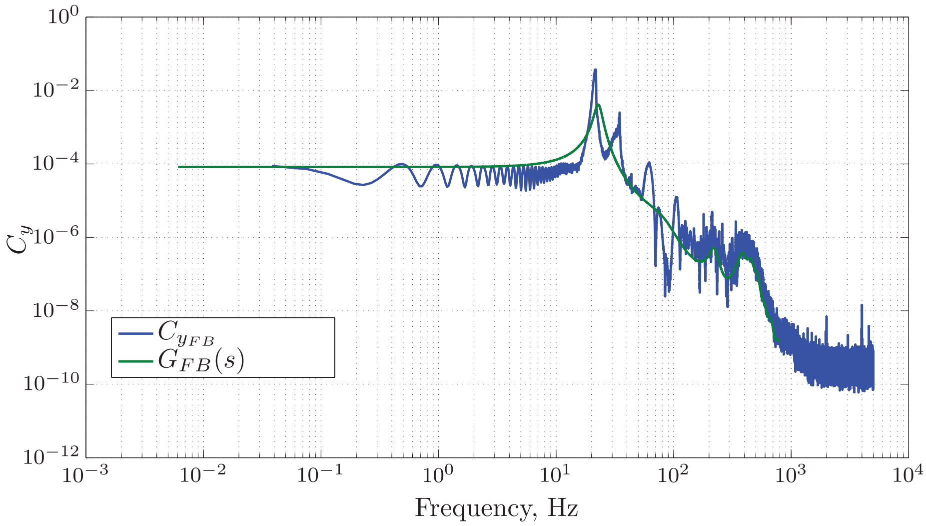


(a)

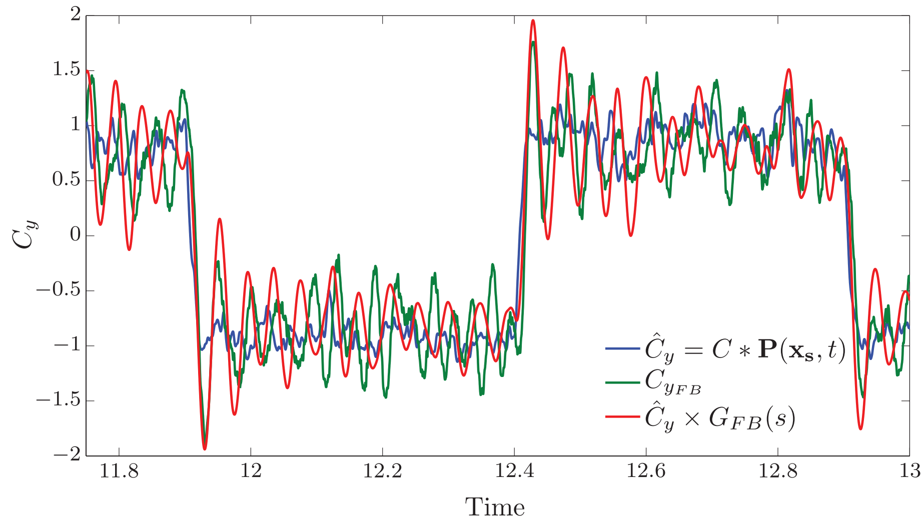


(b)

Figure 7: (a) Frequency spectrum of the side force measurement due to an impulse response [blue] and 8th order AR model [green]. (b) Time domain measurement of side force coefficient [green], estimated side force from pressure signals [blue] and estimated side force measurement when coupled with the dynamics in the AR model [red].

Nonetheless the spectrum shown in Figure 7a allows for modeling of the sensor dynamics. The impulse response of this measurement device is fit by an auto-regressive system in the form,

$$G_{FB}(q)C_{y_{FB}}(t) = e(t) \tag{6}$$

where $C_{yFB}$ is the measurement of the side force and $G_{FB}(q)$ is a frequency domain model of the force balance. All three signals can be compared by the following equation,

$$C_{y_{FB}} \approx G_{FB}(s) * C \times \mathbf{P}(\mathbf{x_s}, t). \tag{7}$$

An example of these signals due to alternating port and starboard forcing is shown in Figure 7b. The green curve represents the actual side force measurement. The experimental measurements of the force balance are compared directly to the pressure based estimates of the force as shown in (Eq) 5. Figure 7b shows the actual force measurements in green, the estimated side force from the linear combination of pressure signals in blue, and the estimated force measurement with the force balance dynamics included in red. As shown qualitative agreement exists between all three signals; the determination is thus that the estimated side force $\hat{C}_y$ is a more suitable signal for the actual force on the model, because the sensor dynamics of the force balance are excluded.

### 3.2 Modeling

The system with the characteristics shown in Figure 5 is suitable for being modeled by a linear system with saturation points as well as a dead zone. Therefore, standard linear system identification methods can be used for the system identification to extract critical features such as delay time, rise time, cut-off frequency, phase/gain margin and minimum phase behavior. Once these critical features are well quantified, the linear system will provide the means for closed-loop controller development. For the open-loop database, the plasma actuator voltage is varied in different manners to fully describe and model the dynamics. In this experimental investigation three separate campaigns were conducted to develop the open-loop database. For training the model, a step response is measured, which contains all necessary information for a linear model to be developed. Linear modeling methods, such as the output error, prediction error and subspace identification methods are implemented to capture the dynamic response to the step input. For validation of the developed model, both impulse and sinusoidal forcing responses are compared to experimental validation.

Initially, due to geometric asymmetries, angular misalignments or flow imperfections the system is in the port asymmetric state which causes a port attached vortex, i.e. a negative $C_y$ or $\Delta C_P$. This steady state value is removed and relative changes to the asymmetric state are analyzed. For all modeling purposes the side force estimate, $\hat{C}_y$, will be used. Also, for all of the data presented, only the port (negative voltages) and starboard (positive voltages) actuators are employed to influence the flow state.

#### 3.2.1 Training Data

The response of the asymmetric vortex state due to a plasma actuation step input is used to develop a linear time invariant model. The step response test campaign consisted of a modulated square wave at a frequency of 1 Hz for a total of 20 periods. The data was then phase averaged over a test duration of 20 seconds to reduce measurement noise. The amplitude of the step was at maximum operational voltage of 12 kV before the amplifier began displaying non-linear effects. Figure 8 shows the normalized response to the step input at initial transient times and Figure 9 for the ending transient times.

The overall time delay consists of the convective time delay for the disturbance to reach the sensor location, lag time for the fluid to respond, and transition time to achieve 90% of the steady-state value. To decouple each of these sources of delay, the convective time delay is defined as the time from which the step begins to the time at which a 10% change in the unforced steady-state value is observed. The rise time is defined as the time from a 10% change in the unforced steady state value to the time at which 90% of the forced steady-state value was achieved. The time responses are then normalized by the flow through time, $\frac{L_{cone}}{U_\infty}$, such that the non-dimensional time vector becomes,

$$\tau = \frac{L_{cone}t}{U_\infty}, \tag{8}$$

For one flow through time, $\tau$ = 1, the corresponding dimensional time was measured to be approximately 13 ms at the current operating conditions. These times are summarized for the rising and falling transients in Table 1. The lag time or presence of non-minimum phase are difficult issues to decouple in the dynamics so further analysis techniques are necessary.

As shown in Table 1, the convective times for a port to starboard or vice versa are very consistent, as expected. The rise or transition time from starboard to port is a bit faster than the transition time from port to starboard. This is, arguably, because the initial asymmetric state prefers the port side due to geometry imperfections, flow misalignments, etc.; thus the flow prefers transition back to the port state and induces a restoring force, reducing transient time and also causing a larger overshoot of the steady state value. Nonetheless, the dynamics of the asymmetric vortex problem as shown by the step response are very well represented by a linear time invariant system.

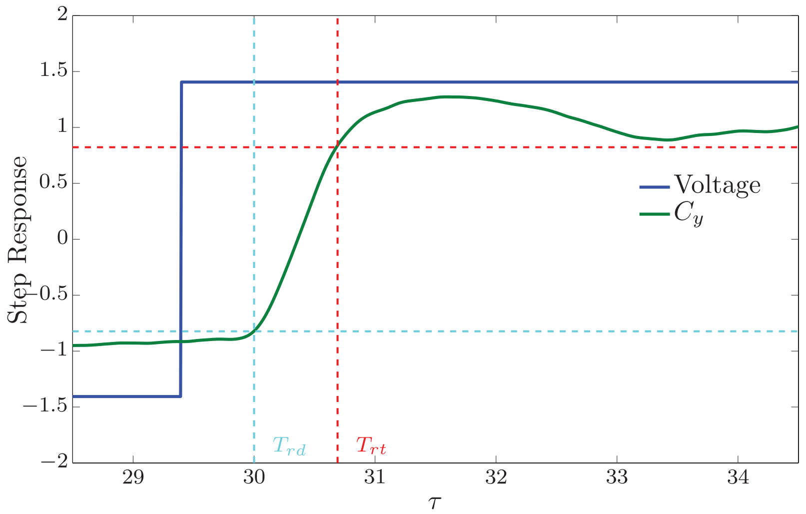


Figure 8: Initial transient of the vortex state due to step input. Linear combination of pressure measurements at $x/D = 2$ and $x/D = 3$ to estimate the side force shown in green. Blue shows the step change of the actuation input in kV. Also, the convective delay time, $T_{rd}$, is shown in cyan and the transition/rise time, $T_{rt}$, is shown in red.

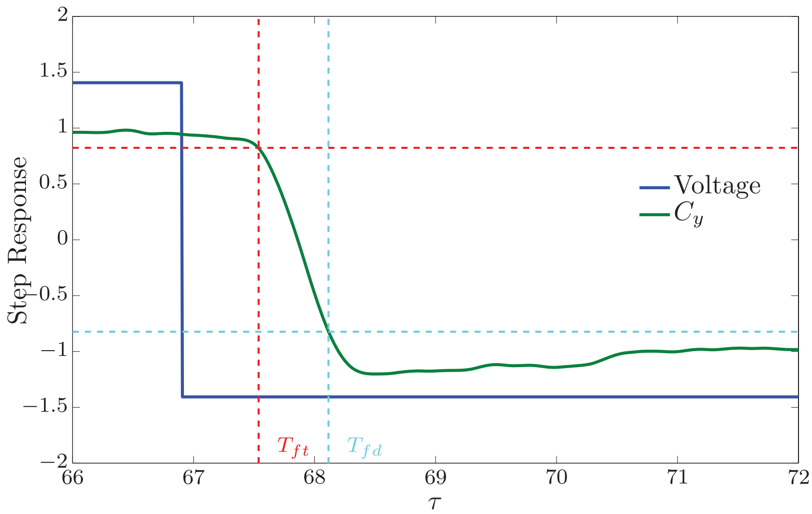


Figure 9: Ending transient of the vortex state due to step input. Linear combination of pressure measurements at $x/D = 2$ and $x/D = 3$ to estimate the side force shown in green. Blue shows the step change of the actuation input in kV. Also, the convective delay time, $T_{fd}$, is shown in cyan and the transition/rise time, $T_{ft}$ , is shown in red.

Table 1: Rise and fall time summary

| | Initial Transient (Port - Starboard) Time [$\tau$] | | | | Ending Transient (Starboard-Port) Time [$\tau$] | | | |
|---|---|---|---|---|---|---|---|---|
| | Delay Time | Rise Time | Total | % Overshoot | Delay Time | Rise Time | Total | % Overshoot |
| $\hat{C}_y$ | 0.6375 | 0.69 | 1.3275 | 18.5 % | 0.6070 | 0.57 | 1.177 | 24.4% |

### 3.2.2 Model Development

The system response is modeled using a linear system parametrization. The input output relationship for this system is

$$Y(s) = G_s(s)U(s). \tag{9}$$

The structure of the model in continuous time will take the form,

$$G_s(s) = \frac{N(s)}{D(s)} = Ke^{\theta s}\frac{s^m + a_{m-1}s^{m-1} + a_{m-2}s^{m-2}\cdots a_1 s + a_0}{s^n + b_{n-1}s^{n-1} + b_{n-2}s^{n-2}\cdots b_1 s + b_0} \tag{10}$$

for a linear system with $m$ zeros and $n$ poles and a pure time delay, $e^{\theta s}$. Different system identification techniques exist for parameterizing suitable orders $G(s)$ and solving for coefficients of the polynomials in numerator and denominator. The three techniques for time domain identification which are examined in this effort are: Output Error (OE), Prediction Error (PEM), and Subspace Identification (SSID) methods.

**Output Error Method** The output error method is an autoregressive exogenous input (arx) model structure, and the identification method is well representative of discrete time and frequency domain data of the form,

$$y(k) = \frac{B(q)}{F(q)}u(k - n_k) + e(t). \tag{11}$$

The OE method minimizes the cost function

$$\|y(k) - \hat{y}(k|\theta)\|_2^2, \tag{12}$$

given a parameterized vector which contains numerator order, denominator order and pure time delay, $n_B$, $n_F$, $n_k$, respectively. The optimal parameter vector, $\hat{\theta}$ is given by

$$\hat{\theta} = \min \frac{1}{N}\sum_{k}^{N-1} \|y(k) - \hat{y}(k|\theta)\|_2^2, \tag{13}$$

For this study the pure, convective time delay is estimated from the step response measurements as shown in Table 1. Six values for $n_k$ are chosen for these formulations. The true pure delay time is shown to be 8 ms with a sample time of $T_s$ = 0.1 ms which corresponds to a discrete delay time of $n_k$ = 80. Because convective time and non-minimum phase aren't decoupled, the convective time parameter was varied to allow for the zeros to adjust accordingly to any non-minimum phase behavior. Both the numerator orders, nB , and denominator orders, nF , are chosen over a range from 1 to 5. With these three parameter ranges, a total of 150 OE models were compared and validated.

**Prediction Error Method** The prediction error method (PEM) has a model structure given by an autoregressive moving average (arma) system, and is an iterative identification approach for multi-input multi-output time domain data with a model structure of the form

$$A(q)y(k) = \frac{B(q)}{F(q)}u(k - n_k) + \frac{C(q)}{D(q)}e(t). \tag{14}$$

This linear time model incorporates a system disturbance term which is filtered by the $\frac{C(q)}{D(q)}$ transfer function (a type of moving average). The parametrization for this model structure consisted of a total of six parameters as shown by,

$$\theta = [n_a, n_b, n_c, n_d, n_f, n_k,]^T , \tag{15}$$

where each numerator and denominator order is denoted by $n_i$. Each order was varied from 1 through 5 and the delay term was set to the convective time delay computed from the step input which was approximately 8 ms. All models were compared and validated against experimental validation data in following sections.

**Subspace Identification Method** The subspace identification (SSID) method is widely used for black box modeling of linear dynamical systems directly in the state space domain, which are written as,

$$\begin{aligned} x_{k+1} &= Ax_k + Bu_k + Ke_k, \\ y_k &= Cx_k + Du_k + e_k, \end{aligned} \tag{16}$$

where $u_k$ is the m-dimensional input, $x_k$ is the n-dimensional state, $y_k$ is the l-dimensional output and $K$ is the Kalman gain. The SSID method is highly useful for MIMO systems, because of its numerical robustness, and its model order optimization based on the singular values of the Hankel matrix. On the downside, large data sets are needed to form the block Hankel matrices, known deterministic processes are difficult to implement, and a strong theoretical understanding of observability and controllability is necessary. The basic premise is to form the Hankel matrices of the input-output data set; the observability matrix,

$$\mathcal{O} = \left[C \;\; CA \;\; CA^2 \cdots CA^{n-1}\right]^T , \tag{17}$$

and the reversed controllability matrix,

$$\mathcal{C} = \left[A^{n-1}B \cdots A^2B \;\; AB \;\; B\right]^T , \tag{18}$$

are imbedded within this large input-output Hankel data matrix. An appropriate model order can be estimated by the singular values of this Hankel matrix. Once the model order is selected, system matrices as shown in Eq. (16) can be extracted.

### 3.2.3 Model Selection

The three modeling techniques described in section 3.2.2 are applied to the training data. The RMS error between the predicted response and actual response serves as the figure of merit for model selection. Transient areas where the input contained high frequency changes were weighted more heavily in the calculation of the prediction error. The best model from each reduced order modeling technique was chosen and model order and structure was compared. Model structure was consistent around a 4th or 5th order model. Also, the poles of the models tended to migrate outside the unit circle if the convective time delay was inaccurate; this non-minimum phase behavior allowed for the discrepancy in the time delay of the model.

The results for the best simulated model responses in comparison to experimental measurements of the step response are shown in Figure 10. Initial and ending transients show very good prediction of convective delay as well as rise/fall time constants as shown in Table 1. The dynamics vary slightly differently when the asymmetric state transitions from port to starboard versus from starboard to port. The transient time from starboard to port vortex states is shorter and the overshoot is greater, as Table 1 indicates. This is potentially because the initial state prefers the port asymmetric state which may provide an additional restoring force to the vortex dynamics. The linear approach taken in this paper finds the mean dynamics between each state trajectory as shown by Figure 10. Nevertheless, each of the models replicates the asymmetric vortex dynamics to a step input very well, thus validating the model parameterizations as well as model selection technique.

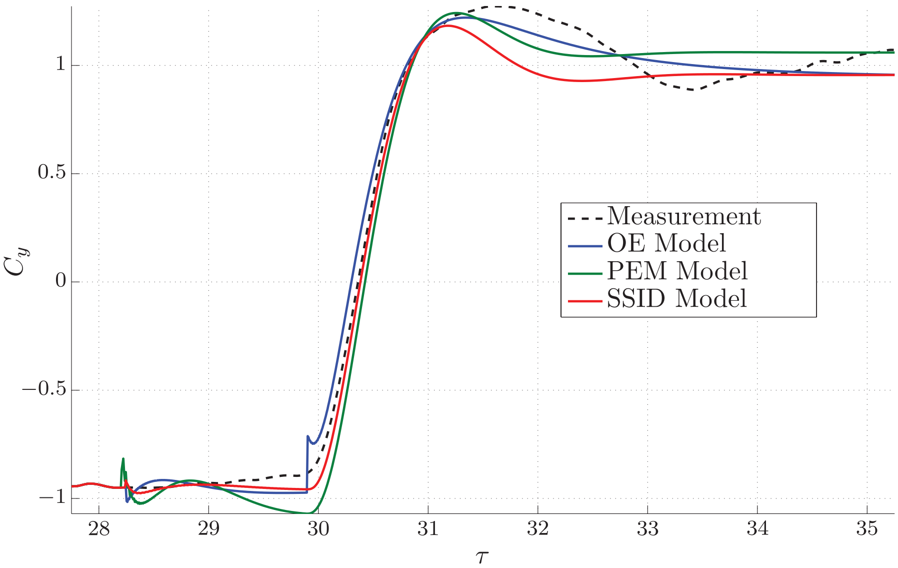


(a)

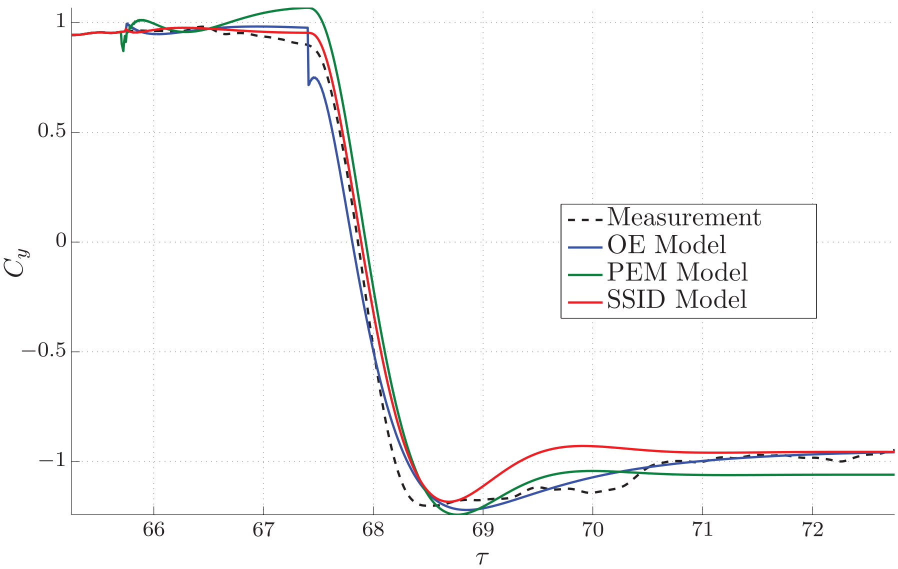


(b)

Figure 10: Step response comparison of OE, PEM, and SSID modeling methods. (a) Initial transient and (b) ending transient of step response of estimated side force, $\hat{C}_y$, based on pressure measurements

### 3.2.4 Validation data

To determine the frequency response of the system dynamics, sinusoidal forcing is used on the port actuator and the system response is observed by the linear combination of all of pressure measurements as given by $\hat{C}_y$. The actuation voltage is modulated by an offset sinusoid, by the equation,

$$A(t) = V_{max}(\sin(2\pi\omega t) + 0.5).$$

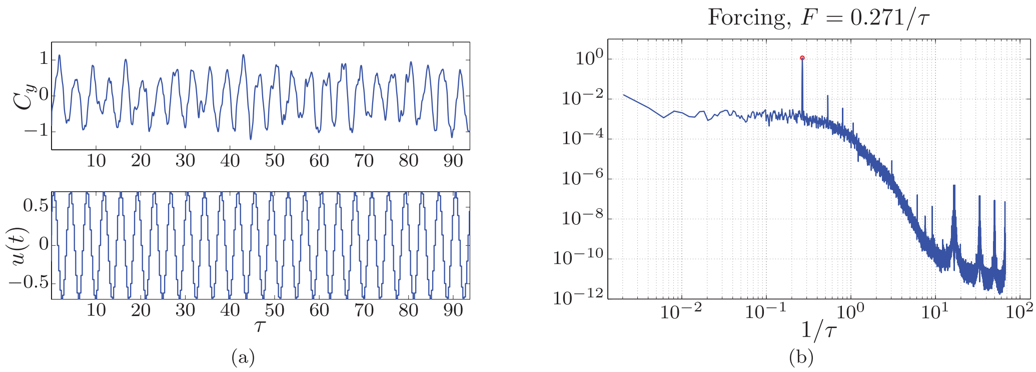


Figure 11: Pressure location $x/D$ = 2 (a) Time domain forcing and response data for Frequency = 20 Hz (b) Time domain forcing and response data for Frequency = 20 Hz.

The test durations consisted of 30 seconds with a sampling frequency of 10 kHz. An example of forcing at a frequency of 20 Hz is shown in Figure 11. The input-output signals are shown as well as the frequency spectrum. Figure 11b shows a large peak at the forcing frequency showing the fluidic receptivity to the forcing. A frequency sweep was conducted over a wide frequency range to determine the cutoff frequency as well as the magnitude and phase of the system.

The natural rise time of the fluidic response is approximately $\tau = 1.1 \rightarrow 1.6$, depending upon port to starboard actuation or vice versa, due to a unit step input as shown in Table 1. The natural frequency is approximately 50 Hz. This suggests that a pole exists near this location. Because of this observation, the modulation frequency was chosen at discrete locations over the range of $0.1\text{Hz} \leq \omega \leq 200\text{Hz}$, to determine magnitude, phase and cutoff frequency.

For all of the forcing frequencies the data is summarized in Figure 12 where the experimental data is plotted in red. From this frequency response information the cutoff frequency can be estimated by a -3 dB attenuation point. This is computed to be approximately 50 $Hz$ and corresponds to a 80 degree phase lag.

The impulse response of the asymmetric vortex state was also measured. For these open-loop tests the duty cycle was varied for a square modulation wave at a frequency of $10Hz$ over a range of 1% to 20%. The experimental measurements are shown below in Figure 13 for the different duty cycles. The initial flow state was shifted to $C_y = 0$, i.e. the symmetric state for modeling purposes. All of the impulses were initiated at $t = 0$, so that the flow response is aligned for each duty cycle. These measurements were phase averaged over 100 total cycles. The results in Figure 13 are well depicted by a linear system. As the duty cycle increases beyond 10% an amount of undershoot is seen by the vortex dynamics. This data set is used completely as validation for the model formulation and model selection technique.

### 3.2.5 Model Validation

The validation data sets were also used to evaluate model performance. The models were calculated against both of the sinusoidal forcing and impulse forcing inputs. The response of the asymmetric state and model responses were compared. Figure 12a shows the summary of the frequency response data which aligns well with the raw frequency measurements. The phase relationship is also shown in Figure 12b. To select between the three different model development approaches, the error is minimized in the frequency domain. The output error technique most adequately fits the frequency domain data, in both magnitude and phase.

Interestingly, the cutoff frequency of the system which is determined from a 90 deg phase is approximately $1/\tau = 1/2$. This means more or less that any frequencies larger than an associated period of two flow through times will be greatly attenuated. This is shown in Figure 12a.

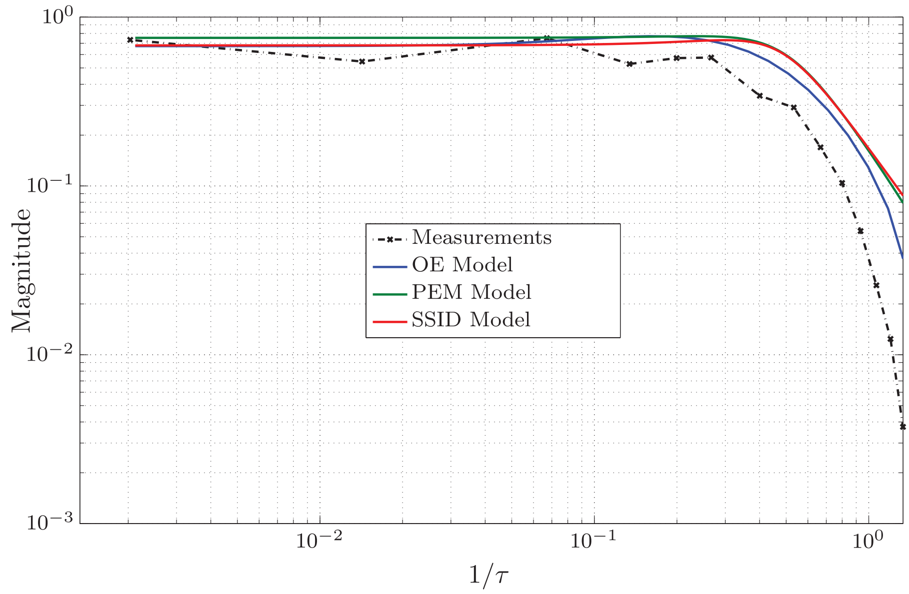


(a)

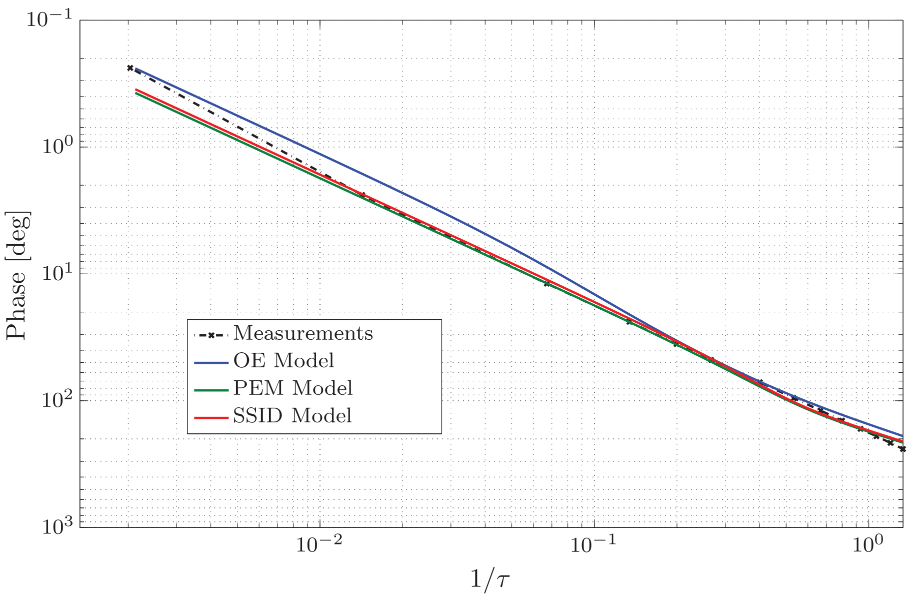


(b)

Figure 12: Comparison of model frequency response and experimental measurements.

Figure 13 shows the impulse response with varying duty cycles for the experimental and simulated output error model results. The various colors represent the different duty cycles. The solid lines represent experimental measurements and the dashed lines represent the OE model prediction. All of the impulses were initiated at time equal to zero with the ending duration of the impulse indicated by a vertical dashed line. The linear model has a slightly different gradient during transient times and a small amount of overshoot when returning to the initial state.

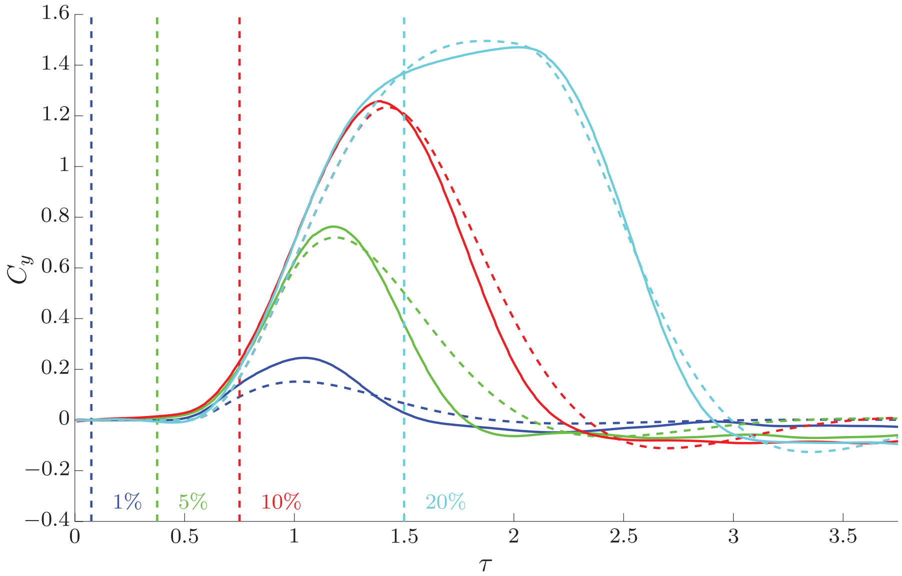


Figure 13: Validation of output error model for simulation of impulse response with varying duty cycles. Model response is shown in dashed line and experimental measurement is shown in solid line

### 3.3. Closed-loop dynamics

Now that the system dynamics in Eq. (9) have been modeled, i.e. the relationship between plasma voltage and estimated side force response is determined, the closed-loop system can be realized. The overall design of the control diagram is shown in Figure 14. The type of control system selected is a reference tracking feed forward approach where $G_s(s)$ is the plant as developed in section 3.2.2, $G_c(s)$ is the control system, and $G_d(s)$ is the output disturbance/measurement noise. The unforced fluid state and measurement noise is modeled by an output disturbance, which is colored by the unforced dynamics of the sensor measurements. The output disturbance, $G_d(s)$, may be represented by the unforced, natural fluctuating state of the flow. An autoregressive model is suitable for the determination of this system. The success of the feedback control scheme will be determined if adequate disturbance rejection as well as reference tracking ability are shown.

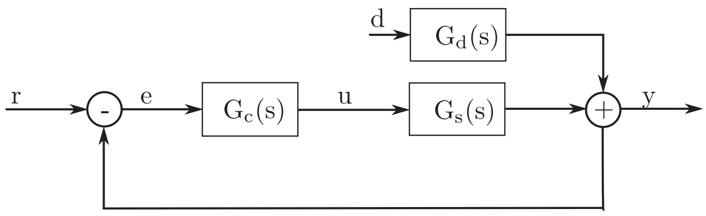


Figure 14: Closed-loop block diagram of output disturbance model for controller verification.

The closed-loop system is formulated such that

$$Y = \begin{bmatrix} \frac{G_s G_c}{1+G_s G_d} & \frac{G_d}{1+G_s G_d} \end{bmatrix} \begin{bmatrix} r \\ d \end{bmatrix}, \tag{19}$$

where $r$ and $d$ are the reference and disturbance inputs, respectively. The transfer function between different input-output pairs can be analyzed for varying forms of $G_c(s)$. For the purpose of this paper, the design of the controller, $G_c\,(s)$, is standard PID control. A PID control algorithm is implemented because of the simplicity and ease of design. The asymmetric vortex dynamics lend themselves very well to linear time invariant systems, so a simple control algorithm is appropriate for control of the vortex flow behind the ogive. The control algorithm is given by

$$G_c(s) = K_p + K_d s + \frac{K_i}{s}, \tag{20}$$

where $K_p$, $K_d$, $K_i$ are the proportional, derivative and integral terms, respectively. A standard tuning method is adopted where the gains are varied in a systematic fashion to achieve proper closed-loop response to a step reference input. The response of $G_s G_c/(1 + G_s G_d)$ is shown for varying proportional and integrator gains in Figure 15. Selected gains for the PI controller are, $K_i = 80$ and $K_p = 1.2$. The derivative term caused an instability in the transfer function, $G_s G_c/(1 + G_s G_d)$, purely due to the time delay in the system. The open loop dynamics can be visualized in the frequency domain as shown in Fig. 16. Here it is calculated that the the open-loop phase margin is 62° and the open-loop gain margin is 2.44 or 7 dB which is suitable from a controls design perspective.

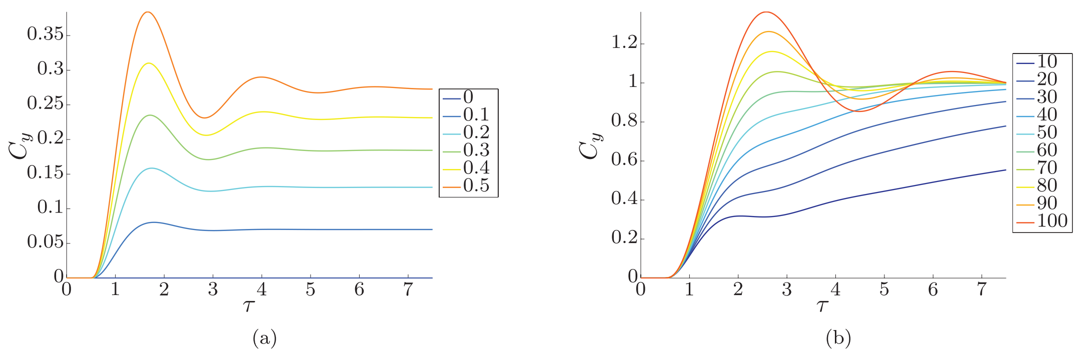


Figure 15: (a) Closed-loop step response with varying proportional gain. (b) Closed-loop step response with varying integral gain.

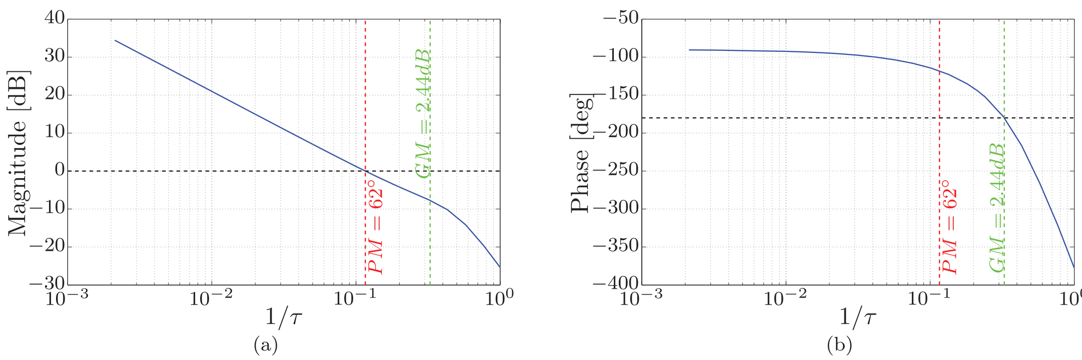


Figure 16: Magnitude (a) and phase (b) response of open loop system, $G_{ol} = G_s G_c$. The gain and phase margins are computed as 2.44dB and 62°, respectively.

The frequency response for the reference tracking and disturbance rejection capabilities are shown in Figure 17. As shown in Figure 17a, the closed-loop system response adequately follows reference signals up to approximately $1/\tau = 1/4$ which was determined to be the cutoff frequency in the open-loop analysis of the dynamics. Figure 17b shows the closed-loop system attenuation of disturbances

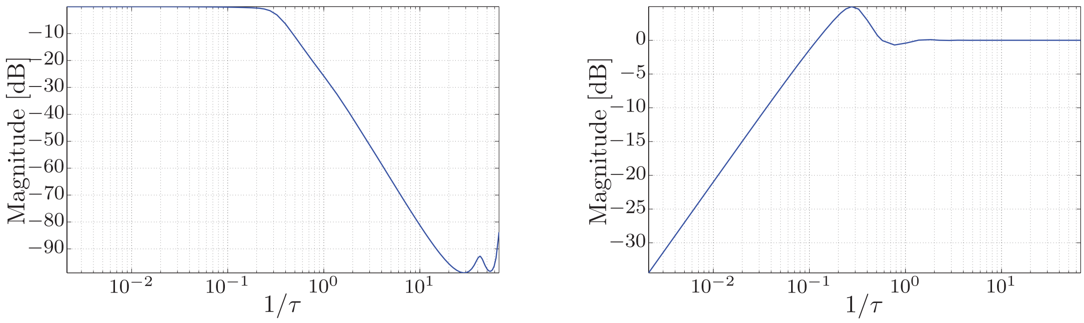


(a) Reference tracking (b) Disturbance rejection

Figure 17: (a) Closed-loop system response for input reference to output response. (b) Closed-loop system response for input disturbance to output response.

(i.e. the ability of the closed-loop system to reduce fluctuations as a function of frequency). Disturbances are attenuated up to a frequency of $1/\tau = 1/10$) i.e. the point at which the amplitude crosses the -3 dB point.

A typical time simulation is shown in Figure 18 to a time varying reference with a uniform random disturbance output. As shown the response of the side force adequately follows a reference signal with a small amount of over shoot and disturbance addition. The controller is designed aggressively enough to have similar transient times in comparison to step inputs in order to maximize the frequency of disturbances rejected/mitigated. This causes overshoot from the following error.

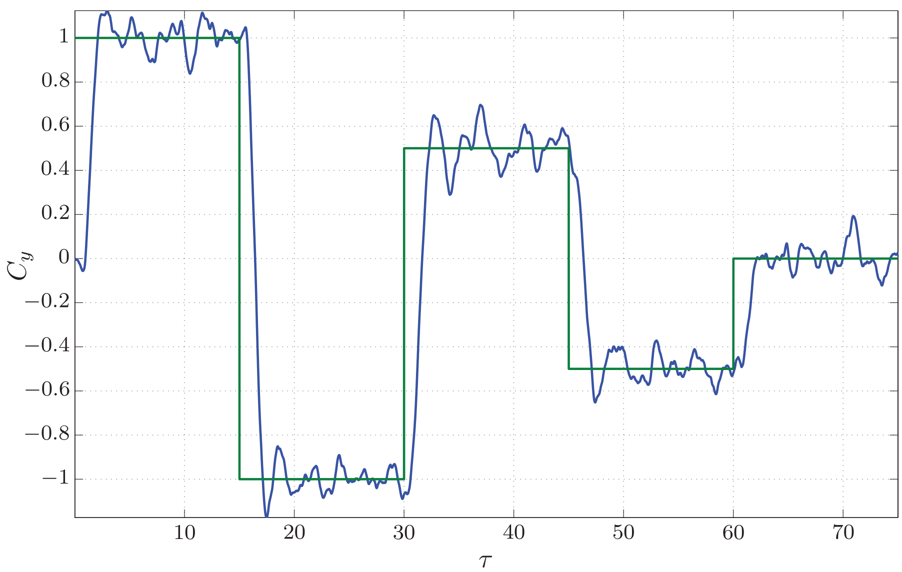


Figure 18: Time simulation of closed-loop system for varying reference and disturbance excitation.

## 4. CONCLUSION

The asymmetric vortex regime of a von Kármán ogive with a fineness ratio of 3.5 is experimentally studied at a Reynolds number of 156,000. Both port and starboard plasma actuators are used to introduce fluidic disturbances at the tip of the ogive. These disturbances are amplified through the flow's convective instability to produce a deterministic port or starboard asymmetric vortex state (i.e. side force). Accurate control or manipulation of this asymmetric vortex phenomenon holds the potential for increased maneuverability and stability characteristics of slender flight vehicles.

Unforced and open-loop experimental tests were carried out to understand and quantify the vortex dynamics. Step, impulse and sinusoidal modulation inputs provided the necessary dynamics and diverse training and validation data sets for the formulation of a linear time invariant dynamical model. Standard linear system identification approaches were implemented to represent the training data set. In particular, output error, prediction error and subspace identification methods were used to capture the asymmetric vortex dynamics. These methods were validated by time and frequency domain methods. The measurements and modeling methods showed the cutoff frequency of the flow to be around 50 Hz which is directly related to two flow through times, i.e. the time it takes a particle to flow from the tip of the model to the base of the ogive section.

A closed-loop system was designed such that the unforced fluid dynamics and measurement noise were modeled as an output disturbance. The prediction error model was well suited for this system. A PID controller was implemented in the closed-loop system and designed for adequate disturbance rejection and reference tracking performance. The closed-loop transfer functions were analyzed. A time simulation was shown in which the controller was able to guide the asymmetric vortex state to an arbitrary asymmetric pressure distribution while adequately regulating the disturbances. To improve this control design approach a predictor model would be essential to reduce the convective time delay from the actuator to the sensor. Alternatively, the sensors would have to be placed closer to the nose of the ogive which would reduce the amplitude of the pressure measurements, reducing the signal to noise ratio.

## REFERENCES

[1] J. E. Bernhardt. *Closed-Loop Control of Forebody Flow Asymmetry*. PhD thesis, Illinois Institute of Technology, 1996.

[2] J. E. Bernhardt and D. R. Williams. Proportional control of asymmetric forebody vortices. *AIAA J.*, 36(11):2087–2093, 1998.

[3] J. E. Bernhardt and D. R. Williams. Closed-Loop Control of Forebody Flow Asymmetry. *J. Aircraft*, 37(3):491–498, 2000.

[4] D. H. Bridges. The asymmetric vortex wake problem - asking the right question. In *AIAA Paper* 2006-3553, 2006.

[5] T. C. Corke, M. L. Post, and D. M. Orlov. SDBD plasma enhanced aerodynamics: concepts, optimiza- tion and applications. *Prog. Aero. Sci.*, 43(7):193–217, 2007.

[6] Y. D. Cui and H. M. Tsai. Side force suppression by dimples on ogive-cylinder body. *AIAA J.*, 47(4):1046–1049, 2009.

[7] L. Darden and N. Komerath. Forebody Vortex Control at High Incidence using a Moveable Nose Stagnation Point. In *AIAA* Paper 1995-1775, 1995.

[8] D. Degani. Effect of geometrical disturbance on vortex asymmetry. *AIAA J.*, VOL. 29, 1991.

[9] X. Deng, G. Wang, X. Chen, Y. Wang, P. Liu, and Z. Xi. A physical model of asymmetric vortices flow structure in regular state over slender body at high angle of attack. *SCIENCE IN CHINA SERIES E-TECHNOLOGICAL SCIENCES*, 46(6):561–573, DEC 2003.

[10] X. Y. Deng, W. Tian, B. F. Ma, and Y. K.Wang. Recent progress on the study of asymmetric vortex flow over slender bodies. *Acta Mech Sin*, 24:475–487, 2008.

[11] M. G. el Hak and C.-M. Ho. Unsteady flow around an ogive cylinder. *J. Aircraft*, 23(6):520–528, 1986. [12] C. Fagley, J. Farnsworth, J. Seidel, and T. McLaughlin. Experimental Study of Open Loop Plasma Actuation on a von Karman Ogive. In *AIAA* Paper 2012-0905, 2012.

[13] C. Fagley, C. Porter, J. Seidel, J. Farnsworth, and T. McLaughlin. Optimal sensor arrangement for asymmetric vortex state estimation on a slender body at high incidence. In *AIAA Aerospace Sciences Meeting, American Institute of Aeronautics and Astronautics*, New Orleans, LA (submitted for publica- tion), 2012.

[14] J. Farnsworth, C. Fagley, C. Porter, J. Seidel, and T. McLaughlin. The transient response of a von karman ogive to open loop plasma actuation. In *AIAA* Paper 2012-2955, 2012.

[15] R. Joussot, D. Hong, R. Weber-Rozenbaum, and A. Leroy-Chesneau. Modification of the Laminar- to-Turbulent Transition on a Flat Plate Using a DBD Plasma Actuator. In *AIAA* Paper 2010-4708, 2010.

[16] E. R. Keener and G. T. Chapman. Side Forces on a Tangent Ogive Forebody with a Fineness Ratio of 3.5 at High Angles of Attack and Mach Numbers from 0.1 to 0.7. Technical report, NASA TM X-3437, 1977.

[17] J. Little, K. Takashima, M. Nishihara, I. Adamovich, and M. Samimy. High Lift Airfoil Leading Edge Separation Control with Nanosecond Pulse Driven DBD Plasma Actuators. In *AIAA* Paper 2010-4256, 2010.

[18] S. C. Luo, K. B. Lua, and E. K. R. Goh. Side force on an ogive cylinder: Effects of surface roughness. *AIAA J.*, 39(4):716–718, 2002.

[19] T. McLaughlin and S. Siegel. USAF Academy Department of Aeronautics Feedback Flow Control Using Plasma Actuators. Number 2 - 22 - 2007, 2007.

[20] T. E. McLaughlin, M. D. Munska, J. P. Vaeth, and S. G. Siegel. Plasma-Based Actuators for Cylinder Wake Vortex Control. 2004.

[21] Y. T. Ng, T. T. Lim, S. C. Luo, and K. B. Lua. Effects of probe interference on side force of an inclined ogive cylinder. *J. Aircraft*, 42(2):420–423, 2003.

[22] M. Patel, C. Tilmann, and T. Ng. Closed-loop missile yaw control via manipulation of forebody flow asymmetries. *J. SPACECRAFT AND ROCKETS*, 41(3):436–443, MAY-JUN 2004.

[23] M. L. Post and T. C. Corke. Separation Control Using Plasma Actuators - Dynamic Stall Control On An Oscillating Airfoil. In *AIAA* Paper 2004-2517, 2004.

[24] D. P. Rizzetta and M. R. Visbal. Numerical Investigation of Plasma-Based Control for Low-Reynolds Number Airfoil Flows. In *AIAA* Paper 2010-4255, 2010.

[25] E. Stephen, N. Carter, C. Leung, C. Sumerel, C.-Y. Hsu, and T. McLaughlin. Flow over a Backward- Facing Step Under Controlled-Plasma Actuator-Induced Perturbations. In *AIAA* Paper 2010-4591, 2010.